

Article

# Microstructure and Properties of High-Entropy $\text{Al}_x\text{CoCrFe}_{2.7}\text{MoNi}$ Alloy Coatings Prepared by Laser Cladding

Minghong Sha <sup>†</sup>, Chuntang Jia <sup>†</sup>, Jun Qiao, Wenqiang Feng , Xingang Ai, Yu-An Jing, Minggang Shen and Shengli Li <sup>\*</sup>

School of Materials and Metallurgy, University of Science and Technology Liaoning, Anshan 114051, China; s13591200297@163.com (M.S.); jia19950608@163.com (C.J.); juncourses@163.com (J.Q.); wqfeng14b@imr.ac.cn (W.F.); aixingang@126.com (X.A.); jyachina@163.com (Y.-A.J.); lnassmg@163.com (M.S.)  
<sup>\*</sup> Correspondence: hongsmh\_116@163.com; Tel.: +86-156-4125-9199

<sup>†</sup> These authors contributed equally to this work.

Received: 25 October 2019; Accepted: 17 November 2019; Published: 20 November 2019



**Abstract:** High-entropy  $\text{Al}_x\text{CoCrFe}_{2.7}\text{MoNi}$  ( $x = 0, 0.5, 1.0, 1.5, 2.0$ ) alloy coatings were prepared on pure iron by laser cladding. The effects of Al content on the microstructure, hardness, wear resistance and corrosion resistance of the coatings were studied. The results showed that the crystal phases of the  $\text{Al}_x\text{CoCrFe}_{2.7}\text{MoNi}$  coatings changed from Mo-rich BCC1 + FCC to (Al, Ni)-rich BCC2 + Mo-rich BCC1 when  $x$  increased from 0 to 0.5, and the phase changed to an (Al, Ni)-rich BCC2 + (Mo, Cr)-rich  $\sigma$  phase as  $x$  increased further. The hardness of the coatings increased as the Al content increased. The  $\text{Al}_{2.0}\text{CoCrFe}_{2.7}\text{MoNi}$  coating exhibit best wear resistance. Addition of Al increased the corrosion potential in a 3.5 wt.% NaCl solution, and the coating with  $x = 1.0$  exhibited the highest corrosion resistance.

**Keywords:** high-entropy alloys; laser cladding; corrosion resistance; wear resistance; microstructure

## 1. Introduction

Yeh et al. [1,2] put forward the concept of a high-entropy alloy (HEA) in 2004, and changed the traditional concept of alloy design. An HEA is defined as an alloy with a configurational entropy larger than  $1.5R$  in the random solution state [3,4], where  $R$  is the gas constant. Owing to their special composition and structure, an HEA exhibits high phase stability, wear resistance, and corrosion resistance [5–12]. Zhang et al. [13] prepared an HEA coating of FeCoCrAlNi on 304 stainless steel by laser cladding. The results showed that the coating exhibits better corrosion resistance and pitting resistance than uncoated 304 stainless steel in a 3.5 wt.% NaCl solution. Niu et al. [14] studied the effect of Al content in an  $\text{Al}_x\text{FeCoCrNiCu}$  ( $x = 0.25, 0.5, 1.0$ ) HEA on its corrosion resistance in a 1 mol/L  $\text{H}_2\text{SO}_4$  solution and a 1 mol/L HCl solution, respectively. The corrosion resistance and pitting resistance in the 1 mol/L  $\text{H}_2\text{SO}_4$  solution increased when the Al content was less than 0.5, while they decreased when the Al content reached 1.0. Kao et al. [15] studied the corrosion resistance of an  $\text{Al}_x\text{CoCrFeNi}$  HEA and found that the corrosion potential ( $E_{\text{corr}}$ ) and corrosion current ( $I_{\text{corr}}$ ) are independent of Al content. Therefore, the effects of Al content on corrosion resistance of HEAs are still not fully understood. An AlCoCrFeNi HEA has been extensively studied for its uncomplicated FCC and BCC phases [16–19]. Some researchers added Ti, Nb, and other elements to the alloy to obtain the desired microstructures, hardness and wear resistance [20–22]. Mo has small thermal expansion coefficient, high strength at high temperatures, high hardness, strong corrosion resistance and high thermal conductivity [23]. It is shown that the addition of Mo increases the strength of AlCrFeNiMo<sub>x</sub>

and  $\text{CoCrFeNiMo}_x$  HEAs due to the formation of the sigma ( $\sigma$ ) phase [24,25]. The  $\sigma$  phase is a hard, brittle phase commonly found in superalloys and can significantly change the mechanical properties of the alloy [26–28]. Its effect on corrosion resistance has not been reported. The effects of Mo content on the structure and properties of  $\text{AlCoCrFeNiMo}_x$  HEAs are being investigated in another of our studies. Due to a higher Fe content in the coating, it is helpful to improve the coating's bond with a steel substrate;  $\text{Al}_x\text{CoCrFe}_{2.7}\text{NiMo}$  HEAs were determined as the coating materials to be studied in our current work.

As a new technology, laser cladding has many advantages over traditional cladding technologies, providing coatings with minimum dilution, minimum deformation, and high surface quality. The effects of Al content on microstructure, hardness, wear resistance and corrosion resistance of  $\text{Al}_x\text{CoCrFe}_{2.7}\text{MoNi}$  coatings prepared by laser cladding were evaluated in this study.

## 2. Materials and Methods

Pure iron was selected as the base material in order to eliminate the effects of other elements. Its high purity allows accurate analysis and characterization of the structure and properties of HEAs. Table 1 shows the chemical composition of the base material measured by chemical analysis.

The pure metal powders used in the experiments are the atomized powders produced by BGRIMM (Beijing, China). Pure powders of Al, Co, Cr, Fe, Ni, and Mo (>99.9%, wt.%) with an average particle size of 75  $\mu\text{m}$  were used as raw cladding materials. The powders were weighed and mixed according to the proportions listed in Table 2 ( $\text{Fe}_{2.7}$  was achieved by appropriate laser parameters determined through multiple test attempts to control the dilution ratio of the coating and the base material). Then, the mixed alloy powder was put into a stainless-steel tank and thoroughly dry blended for 5 h in a planetary ball mill with a rotating speed of 300 r/min. After sieving, placed in a vacuum dries oven to prevent oxidation. A mixed powder layer with 1 mm thickness was placed on the base material and radiated by the laser in an argon atmosphere. Single-pass laser cladding was used to deposit coatings of  $\text{Al}_x\text{CoCrFe}_{2.7}\text{MoNi}$  at 1350 W, 980 nm wavelength, 20 mm/s scanning rate, and 3 mm spot diameter (Laserline LDF 4000, Laserline GmbH, Mülheim-Kärlich, Germany). The radiated samples were then annealed at 900 °C for 5 h to relieve thermal stress and prevent microcrack formation. The structures of the samples were analyzed using X-ray diffraction (XRD, PANalytical X-pert Power, Malvern Panalytical Ltd., Worcestershire, UK) with a line detector (X'Celerator) at  $2\theta$  ranging from 15° to 90° in 0.065° increments with  $\text{Cu K}\alpha$  radiation. High Score Plus software and PDF-2004 database (JCPDS, Newtown Square, PA, USA) were used to analyze the diffraction pattern. The specimens were eroded in aqua regia for 5–10 s, and the morphologies and compositions of the coatings were analyzed using a scanning electron microscope (SEM, Hitachi S-3400N, Hitachi, Ltd., Tokyo, Japan) with an energy dispersive spectrometer (EDS, TEAM PEGASUS2040), and with a transmission electron microscope (TEM, FEI Talos F200, FEI Co. Ltd, Hillsboro, OR, USA) with an EDS (FEI Super X). The size of the investigated area used for the measurements of the overall compositions of coatings in Table 3 is 1300  $\mu\text{m}$   $\times$  265  $\mu\text{m}$ . Microhardness was measured from the bond zone to the coating surface using a microhardness tester (Qness Q10A, Qness GmbH, Golling, Austria) with a 9.81 N loading force and 15 s loading time. The wear resistance was tested with friction and wear test equipment (UMT TriboLab, Bruker Corporation, Billerica, MA, USA) with a pair of ceramic balls. A 13 N normal load, 100 mm/s reciprocating speed, a 10 mm reciprocating straight line distance and 1800 mm total wear distance were used in the wear tests. The weight of the samples before and after wear tests was weighed with a balance (0.01 mg precision). The  $E_{\text{corr}}$  and  $I_{\text{corr}}$  were measured with an electrochemical workstation (Autolab PGSTAT302N) from  $-1.2$  to  $1.2$  V and 1.0 mV/s scanning speed in a 3.5 wt.% NaCl aqueous solution. The  $E_{\text{corr}}$  and  $I_{\text{corr}}$  of the coatings were obtained by Tafel linear extrapolation. A platinum electrode, saturated AgCl electrode and the specimen were used as the auxiliary, reference, and working, respectively. The chemical valence states of metal elements in passive films formed on the surfaces of the  $\text{Al}_{1.0}$  and  $\text{Al}_{2.0}$  coatings were measured using X-ray photoelectron spectroscopy (XPS, Escalab 250Xi, Thermo Fisher Scientific, Waltham, MA, USA) with monochromatic Al  $\text{K}\alpha$  excitation.

**Table 1.** Pure iron content for matrix (wt.%).

Element	Fe	Al	S	P	Mn	Si	C
Content	99.457	0.22	0.014	0.011	0.120	0.150	0.028

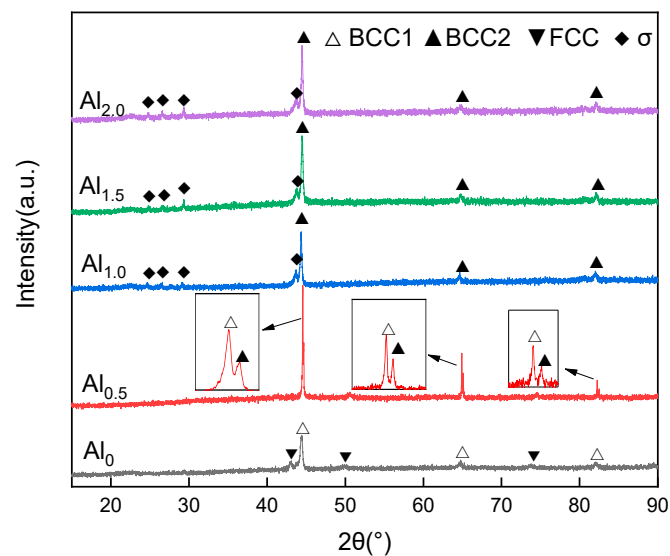
**Table 2.** Composition of the mixed powder (wt.%).

$x$	Al	Co	Cr	Fe	Mo	Ni
0	0	18.34	16.18	17.38	29.85	18.26
0.5	4.03	17.60	15.52	16.68	28.65	17.53
1.0	7.74	16.92	14.92	16.03	27.54	16.85
1.5	11.18	16.28	14.37	15.43	26.51	16.22
2.0	14.38	15.70	13.85	14.88	25.56	15.64

### 3. Experimental Results

#### 3.1. Crystal Structure

X-ray diffraction patterns from the  $Al_xCoCrFe_{2.7}NiMo$  coatings are shown in Figure 1. The coatings are mainly composed of simple solid solutions and intermetallic compounds. The phase structure is composed of both BCC and FCC solid solutions when  $x = 0$ , while BCC1 and BCC2 solid solutions appear and the peak value is more intense when  $x = 0.5$ . Tiny Bragg peaks corresponding to the  $\sigma$  and BCC phases are visible in the XRD pattern when  $x = 1.0$ , and no new phase appears in the XRD pattern as the Mo content increases ( $x = 1.5$  and 2.0).

**Figure 1.** XRD pattern from  $Al_xCoCrFe_{2.7}MoNi$  coatings.

### 3.2. Microstructure

SEM images of the microstructure of the  $\text{Al}_x\text{CoCrFe}_{2.7}\text{MoNi}$  ( $x = 0, 0.5, 1.0, 1.5, 2.0$ ) coatings are shown in Figure 2a–c, e, and g. In view of the fineness of microstructure and the limitations of the SEM, TEM images of the microstructures of  $\text{Al}_{1.0}$ ,  $\text{Al}_{1.5}$ , and  $\text{Al}_{2.0}$  HEAs are presented in Figure 2d, f and h. The target composition and actual composition of the coatings measured by EDS are listed in Table 3. The chemical compositions in different micro-regions of  $\text{Al}_x\text{CoCrFe}_{2.7}\text{MoNi}$  are shown in Table 4. A few precipitates containing Fe and Cr appear in region A of the coating without Al, as shown in Figure 2a. Figure 2b shows that the  $\text{Al}_{0.5}$  coating consists of dendrites. Figure 2c,e,g shows that  $\text{Al}_{1.0}$ ,  $\text{Al}_{2.0}$ , and  $\text{Al}_{3.0}$  alloys have fine microstructures, respectively. The light and dark phases appear in  $\text{Al}_{1.0}$ , indicated by D and C, respectively, as shown in Figure 2d. The EDS results and analysis of the diffraction spots show that the C phase is a Mo-rich  $\sigma$  phase, and the D phase is an (Al, Ni)-rich BCC2 phase. Figure 2f shows that two kinds of dark areas (granules and sheets) and one bright area can be seen in the  $\text{Al}_{1.5}$  coating, indicated by C,  $C_1$ , and D, respectively. An analysis of the diffraction spots show that the C and  $C_1$  phases belong to the (Mo, Cr)-rich  $\sigma$  phase, while the D phase is an (Al, Ni)-rich BCC2 phase. The dark strip disappears as Mo content increases, as shown in Figure 2h, and the microstructure is composed of a granular (Mo, Cr)-rich  $\sigma$  phase and (Al, Ni)-rich BCC2 phase.

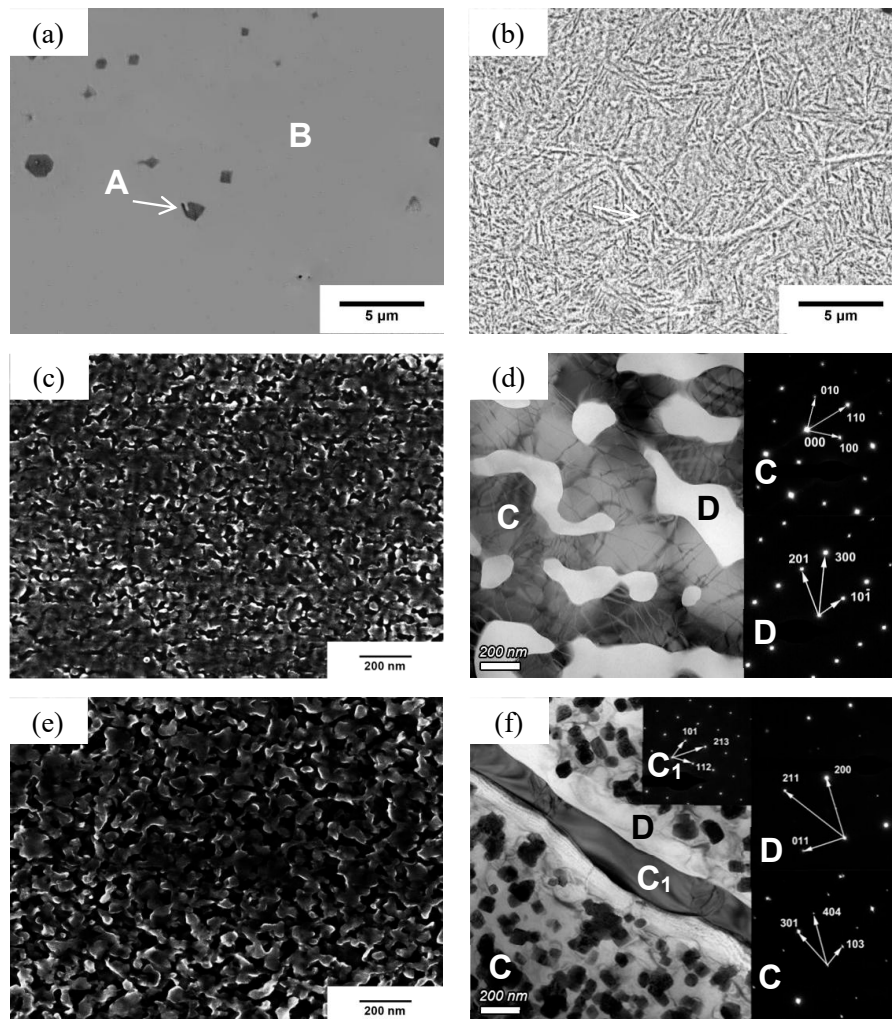
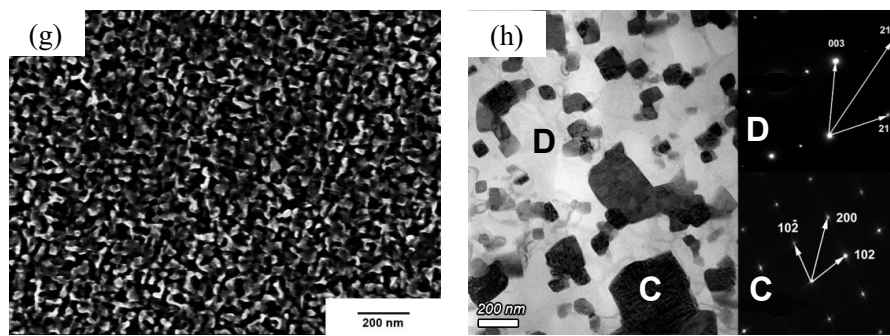


Figure 2. Cont.



**Figure 2.** Microstructures of the  $Al_xCoCrFe_{2.7}MoNi$  coatings. (a–c,e,g) show SEM images; (d,f,h) show TEM images.

**Table 3.** Composition of coatings measured by EDS (at.%).

$x$	Type	Al	Cr	Fe	Co	Ni	Mo
0	Actual	0	14.52	40.39	15.04	16.56	13.49
	Target	0	14.93	40.30	14.93	14.93	14.93
0.5	Actual	5.92	13.73	37.87	14.88	12.82	14.79
	Target	6.94	13.89	37.50	13.89	13.89	13.89
1.0	Actual	12.71	13.25	36.33	12.96	12.76	11.98
	Target	12.99	12.99	35.06	12.99	12.99	12.99
1.5	Actual	16.36	13.93	32.77	12.19	12.81	11.94
	Target	18.29	12.20	32.93	12.20	12.20	12.20
2.0	Actual	19.25	11.34	33.95	11.45	11.69	12.32
	Target	22.99	11.49	31.03	11.49	11.49	11.49

**Table 4.** Composition of coatings micro-regions (at.%).

Alloy	Region	Al	Co	Cr	Fe	Ni	Mo
$Al_{0.0}$	A region	0	0	79.98	20.02	0	0
	B region	0	17.71	13.85	53.28	13.61	7.55
$Al_{0.5}$	D region	5.25	11.91	8.59	53.41	9.24	11.60
	C region	1.76	10	18.2	49.44	2.46	17.75
$Al_{1.0}$	D region	28.91	17.04	1.96	22.17	29.57	0.32
	C region	1.01	8.98	13.72	58.11	2.01	34.89
$Al_{1.5}$	D region	25.60	11.63	3.84	38.55	19.20	1.18
	E region	6.34	7.93	15.87	43.97	3.17	22.68
$Al_{2.0}$	C region	3.53	7.87	15.21	53.58	2.16	17.34
	D region	26.68	12.58	3.84	36.52	19.76	0.58

### 3.3. Microhardness

The microhardness measurements from different positions in the  $Al_xCoCrFe_{2.7}MoNi$  coatings are shown in Figure 3. The  $CoCrFe_{2.7}NiMo$  alloy has the lowest average hardness (272 HV), which can be attributed to generation of the FCC phase. The microhardness increases as Al content increases, and  $Al_{2.0}CoCrFe_{2.7}NiMo$  has the highest average hardness (1142 HV). Hardness test results show that the formation of the BCC2 phase increases the hardness of the coating.

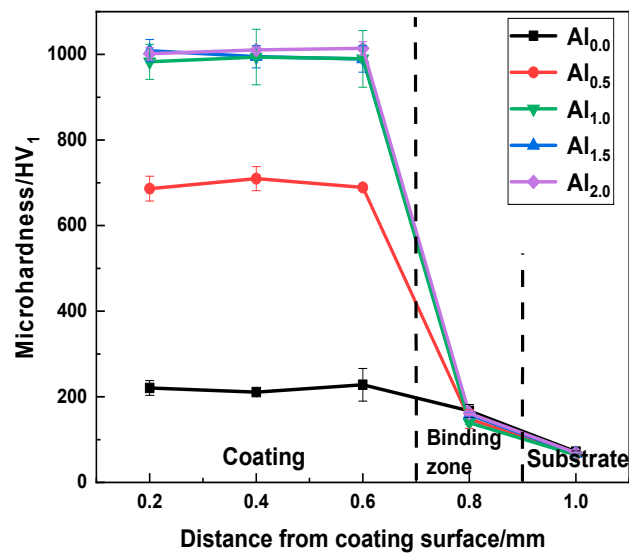


Figure 3. Microhardness of  $\text{Al}_x\text{CoCrFe}_{2.7}\text{MoNi}$  coatings.

#### 3.4. Wear Resistance

Wear in a material is related to its structure and external environment. The wear resistance of samples  $\text{Al}_{1.0}$ ,  $\text{Al}_{1.5}$ , and  $\text{Al}_{2.0}$  was analyzed in this paper. The morphology of worn  $\text{Al}_x\text{CoCrFe}_{2.7}\text{MoNi}$  ( $x = 1.0, 1.5, 2.0$ ) coatings is shown in Figure 4a–c. Figure 4a–c, respectively. There is a convex scaly plastic deformation layer on the friction surface of the  $\text{Al}_{1.0}$  sample, as shown in Figure 4a,a<sub>1</sub>, which resulted from repeated grinding during the wear test. An oxide developed at the junction of the flaky furrow and the scaly deformed layer because of severe friction and high temperature during the wear test. The wear mechanism is mainly adhesive wear and oxidative wear. The wear of the  $\text{Al}_{1.5}$  sample is with a few flake furrows, in which oxides were found, as shown in Figure 4b,b<sub>1</sub>, indicating the wear occurs via oxidation, slight adhesion wear and slight abrasive wear. Sample  $\text{Al}_{2.0}$  also exhibits a scaly plastic deformation layer with oxides and a flaky furrow in Figure 4c,c<sub>1</sub>. The wear mechanism in sample  $\text{Al}_{2.0}$  is adhesive wear and oxidative wear. The measured weight losses from the coatings due to wear are listed in Table 5; sample  $\text{Al}_{2.0}$  exhibited the least wear of 0.1 mg.

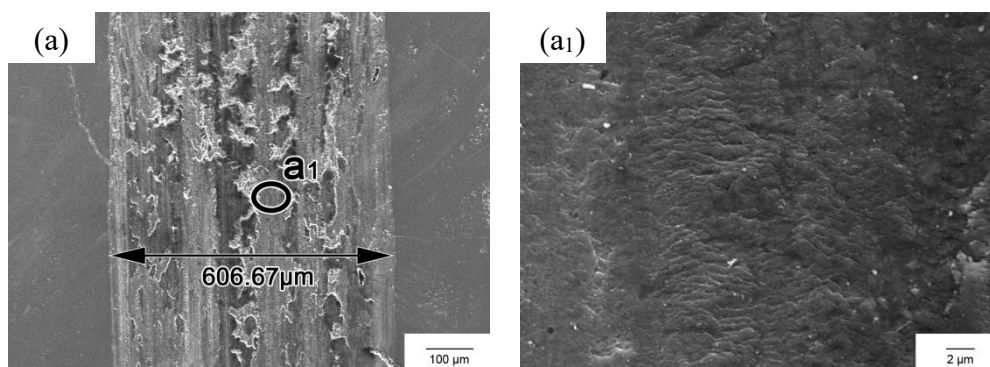
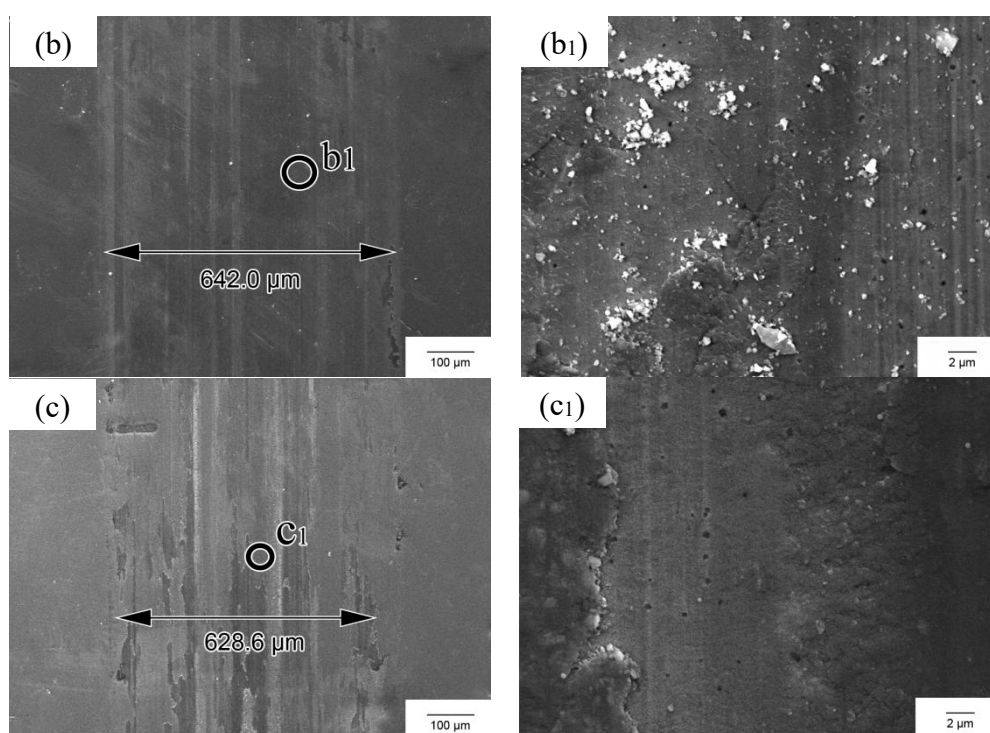


Figure 4. Cont.



**Figure 4.** Wear morphology of the  $\text{Al}_x\text{CoCrFe}_{2.7}\text{MoNi}$  ( $x = 1.0, 1.5, 2.0$ ) coatings; (a,a<sub>1</sub>)  $x = 1.0$ ; (b,b<sub>1</sub>)  $x = 1.5$ ; (c,c<sub>1</sub>)  $x = 2.0$ .

**Table 5.** Weight loss from the  $\text{Al}_x\text{CoCrFe}_{2.7}\text{MoNi}$  ( $x = 1.0, 1.5, 2.0$ ) coatings.

Alloy	Before Abrasion/g	After Abrasion/g	Abrasion Weight Loss/mg
Al <sub>1.0</sub>	10.0048	10.0044	0.4
Al <sub>1.5</sub>	8.4143	8.4141	0.2
Al <sub>2.0</sub>	10.1304	10.1303	0.1

### 3.5. Corrosion Resistance

Potentiodynamic polarization curves of the  $\text{Al}_x\text{CoCrFe}_{2.7}\text{MoNi}$  coatings in the 3.5 wt.% NaCl solution are shown in Figure 5. The  $E_{corr}$  and  $I_{corr}$  of the coatings were obtained by Tafel linear extrapolation, as shown in Table 6. These results show that, except for sample Al<sub>1.0</sub>, the self-corrosion potential of the other coatings increases as the Al content increases. The self-corrosion current density with sample Al<sub>1.0</sub> is the least, while the self-corrosion current density with samples Al<sub>1.5</sub> and Al<sub>2.0</sub> are slightly larger. Sample Al<sub>0.0</sub> exhibits the lowest self-corrosion potential and higher self-corrosion current density, indicating that it has the greatest corrosion tendency, highest corrosion rate and worst corrosion resistance. Figure 6 shows XPS results from passive films on the  $\text{Al}_x\text{CoCrFe}_{2.7}\text{NiMo}$  ( $x = 1.0, 2.0$ ) coatings after the corrosion experiments in the 3.5 wt.% NaCl solution. The composition of the passive film is  $\text{Al}_2\text{O}_3$ ,  $\text{CoO}$ ,  $\text{Co}_2\text{O}_3$ ,  $\text{Cr}_2\text{O}_3$ ,  $\text{Fe}_2\text{O}_3$ ,  $\text{MoO}_3$ , and  $\text{NiO}$  when  $x = 1.0$ , while the passive film is primarily composed of  $\text{Al}_2\text{O}_3$ ,  $\text{CoO}$ ,  $\text{Cr}_3\text{O}_4$ ,  $\text{Fe}_2\text{O}_3$ ,  $\text{MoO}_3$ , and  $\text{NiO}$  when  $x = 2.0$ .  $\text{Al}_2\text{O}_3$ ,  $\text{Cr}_2\text{O}_3$ ,  $\text{CoO}$ ,  $\text{MoO}_3$ , and  $\text{NiO}$  were detected on the surfaces of all coatings, which can provide certain protection in a corrosive environment. The compositions (in relative at.%) of the passive films determined from XPS measurements are summarized in Figure 7. This shows that the content of  $\text{Al}_2\text{O}_3$  is higher than that of other metal oxides, and the relative contents of Ni, Co and Fe oxides decrease as the Al content increases. This is primarily due to the fact that Al is active and oxidizes easier than the other elements listed here.

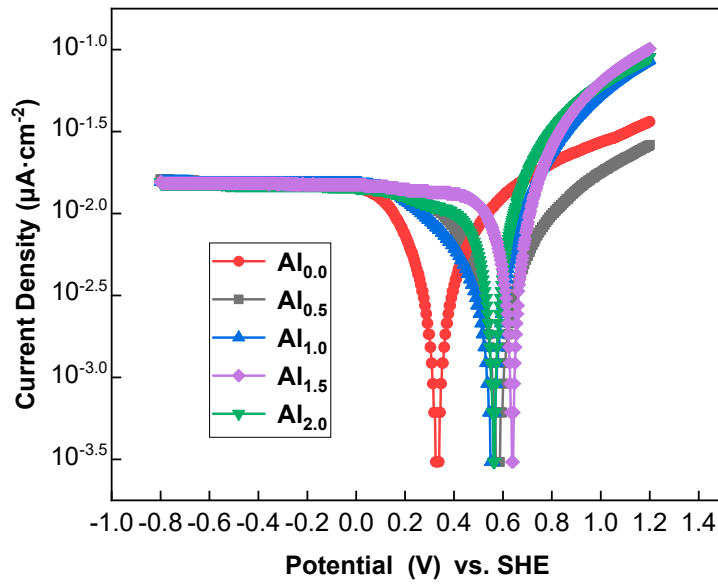


Figure 5. Polarization curves of  $Al_xCoCrFe_{2.7}MoNi$  coatings in a 3.5 wt.% NaCl solution.

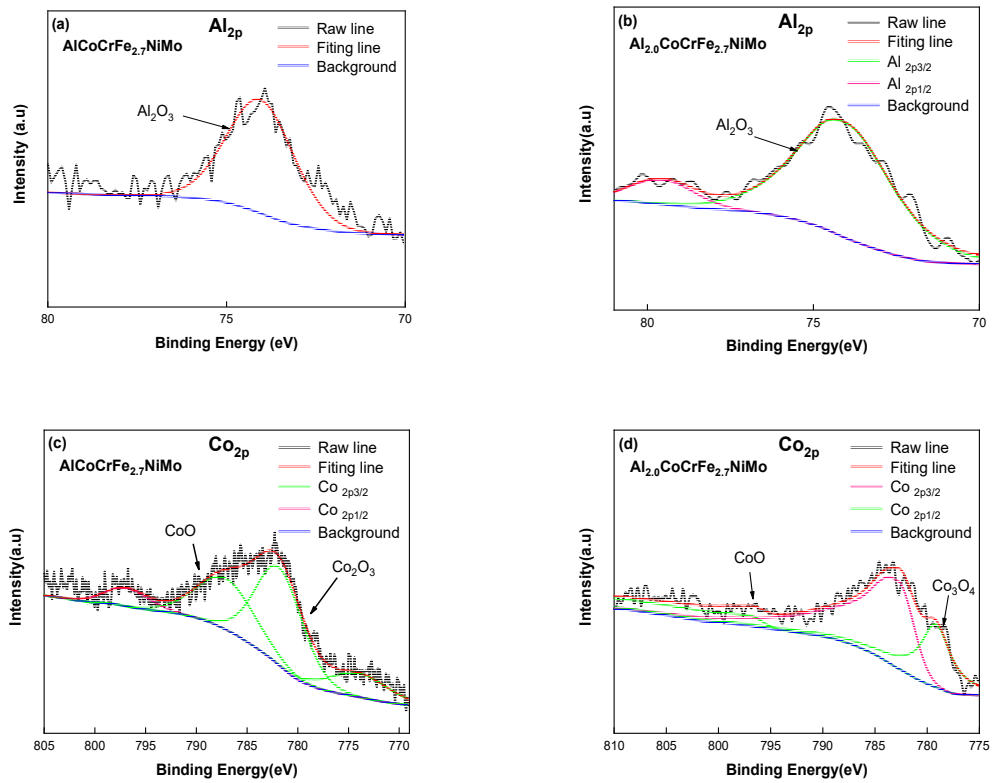


Figure 6. Cont.

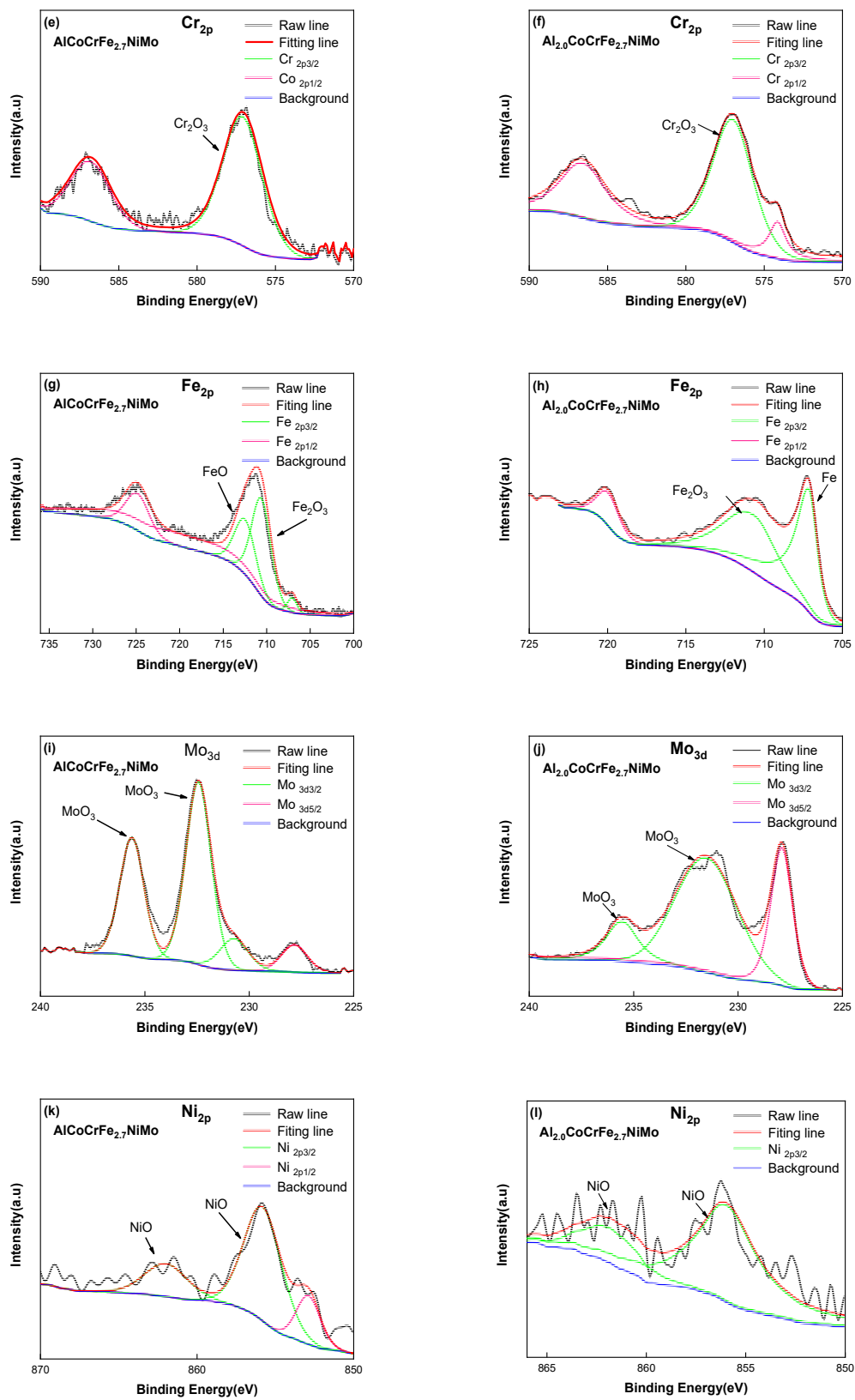
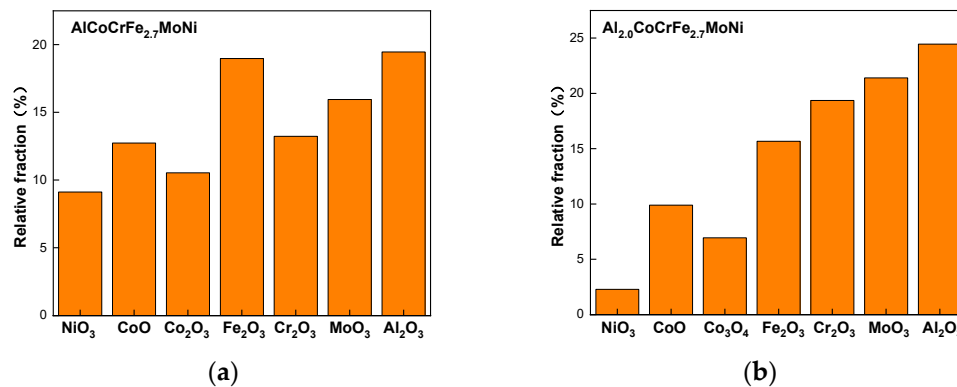


Figure 6. XPS spectra from the passive film formed on the surfaces of the coatings. (a,c,e,g,i,k)  $x = 1.0$ ; (b,d,f,h,j,l)  $x = 2.0$ .



**Figure 7.** Composition (in relative at.%) of the surface of Al<sub>1.0</sub> and Al<sub>2.0</sub> coatings determined from XPS measurements. (a)  $x = 1.0$ ; (b)  $x = 2.0$ .

**Table 6.** Measured electrical behavior during corrosion of the Al<sub>*x*</sub>CoCrFe<sub>2.7</sub>MoNi coatings in a 3.5 wt.% NaCl solution.

Alloys	$I_{corr} / \mu\text{A}\cdot\text{cm}^{-2}$	$E_{corr}$ vs. SHE/V
Al <sub>0.0</sub>	$2.033 \times 10^{-3}$	0.332
Al <sub>0.5</sub>	$1.803 \times 10^{-3}$	0.581
Al <sub>1.0</sub>	$1.355 \times 10^{-3}$	0.556
Al <sub>1.5</sub>	$2.364 \times 10^{-3}$	0.639
Al <sub>2.0</sub>	$2.762 \times 10^{-3}$	0.586

## 4. Discussion

### 4.1. Microstructure and Phase

Results in many studies have shown that the CoCrFeNi alloy consists of a single FCC phase [26,29,30]. Our XRD analysis results show that the CoCrFe<sub>2.7</sub>NiMo alloy consists of FCC and BCC phases (as shown in Figure 1), which indicates that adding Mo causes formation of the BCC1 phase. This conclusion is consistent with Wu's research [29]. Table 7 shows the enthalpy of mixing between elements. The enthalpy of mixing between Fe and Cr is relatively higher, and it is difficult to form a stable solid solution. Therefore, it is considered that the high melting point of the mixed powders leads to incomplete melting while depositing an Al<sub>0</sub> alloy. The enthalpy of mixing between Al and other elements is lower than that between Mo and other elements, and results from many studies show that adding Al can cause the FCC phase to change to the BCC phase in HEAs [30–32]. Therefore, the FCC phase disappears in the Al<sub>1.0</sub> alloy and the peak in the XRD pattern becomes more intense due to the increased BCC phase content (BCC1 phase and (Al, Ni)-rich BCC2). Elements such as Co, Ni and Al enrich to form a disordered (Al, Ni)-rich BCC2 phase (random solid solution) as the Al content increases further, as shown in Figure 8a. Meanwhile, Mo dissolves with other elements, e.g., Ni, to form an ordered  $\sigma$  phase (intermetallic), as shown in Figure 8b. A random solid solution tends to have a large configuration entropy due to random mixing of its various elements [1,2]. According to the Gibbs free energy formula  $G = H - TS$  ( $G$  is the Gibbs free energy,  $H$  is the enthalpy of mixing,  $T$  is the temperature, and  $S$  is the configuration entropy).  $G$  is negative when  $S > (H/T)$  and the solid solution phase forms easily, and the enthalpy of mixing between Al and other elements is lower than that between Mo and other elements, indicating that other elements dissolve more easily in Al than Mo, forming a solid solution, as shown in Table 7 (the data are derived from the literature [33]). Therefore, the addition of Al generates a large amount of the (Al, Ni)-rich BCC phase, which forces the Mo-containing BCC1 phase to transform into a (Mo, Cr)-rich  $\sigma$  phase. In conclusion, for the alloys studied herein, Mo allows a BCC structure to form more easily when Al is absent in the coating, while

both Al and Mo easily form a BCC structure when a small amount of Al is added. Al is the primary driver of BCC formation, and addition of Mo tends to cause formation of the  $\sigma$  phase when more Al is added.

**Table 7.** Mixing enthalpy values for different element pairs, data from [33].

Element	$\Delta H_{AB}^{\text{mix}}$					
	Al	Co	Cr	Fe	Ni	Mo
Al	-					
Co	-19	-				
Cr	-10	-4	-			
Fe	-11	-1	-1	-		
Ni	-22	0	-7	-2	-	
Mo	-5	-5	0	-2	-7	-

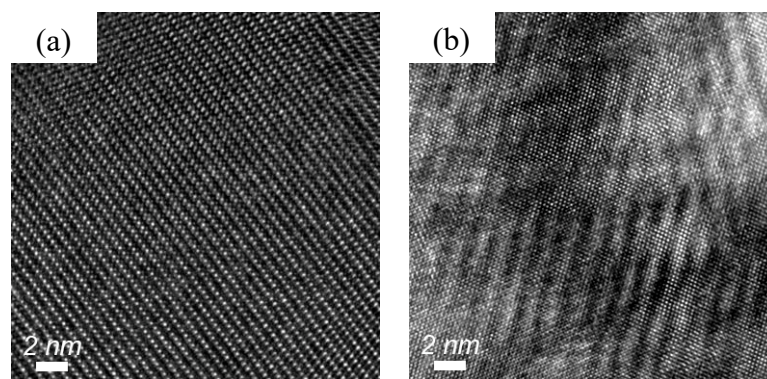


**Figure 8.** High resolution TEM images of the  $\sigma$  and BCC phases in the AlCoCrFe<sub>2.7</sub>NiMo coating. (a) shows  $\sigma$  phase; (b) shows BCC phase.

#### 4.2. Hardness and Wear Resistance

Hardness and wear resistance of alloys are closely related to their microstructures. Figure 9 shows the relationship between the volume fraction of the phases in the coating, obtained by XRD and the hardness of the coating. The presence of the FCC phase minimizes the hardness of the Al<sub>0</sub> alloy, and formation of (Al, Ni)-rich BCC2 causes the hardness of the Al<sub>0.5</sub> alloy to increase. The volume fraction of BCC2 phase has a greater influence on the hardness and wear resistance of the coatings than does that of  $\sigma$  phase. Greater content of the (Al, Ni)-rich BCC2 phase correlates with higher hardness and wear resistance as the Al content increases. However, the presence of the flaky  $\sigma$  phase causes large flaky exfoliation on the Al<sub>1.0</sub> coating in wear resistance experiments, which can be attributed to the brittleness of the  $\sigma$  phase. It is worth noting that the  $\sigma$  phase changes from sheet-like to granular as the Al content increases further, which plays a role of dispersion strengthening in the alloy. Furthermore, plastic deformation can be observed in the wear microstructure diagram of the Al<sub>1.0</sub> coating, while no plastic deformation can be observed in the Al<sub>1.5</sub> and Al<sub>2.0</sub> coatings. Oxides appear, which indicates that oxidation wear is the primary wear mechanism, and dispersion strengthening can significantly increase the coating's wear resistance. In summary, introduction of the (Al, Ni)-rich BCC2 phase increases the hardness and wear resistance of the coating. Adding Al reduces the size of the  $\sigma$  phase, which also increases the hardness and wear resistance of the coating.

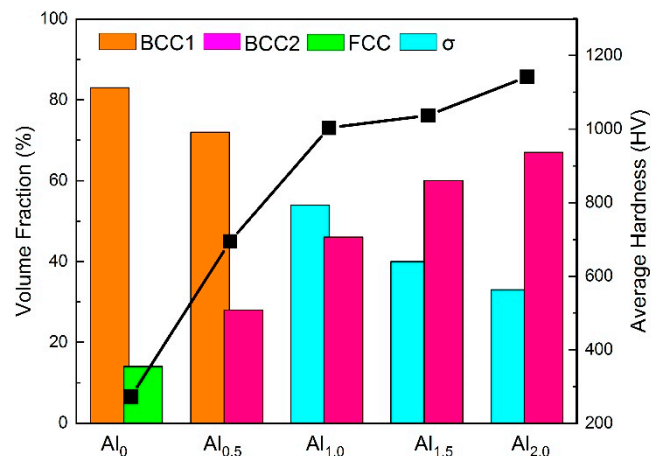


**Figure 9.** Relationship between the volume fraction of the phases and the average hardness of the coatings.

#### 4.3. Corrosion Resistance

Figure 10 shows a comparison of  $E_{corr}$  and  $I_{corr}$  in our  $Al_xCoCrFe_{2.7}NiMo$  coatings and  $Al_xCoCrFeNi$  alloys from the literature [34]. One can see that the addition Mo leads to increased corrosion resistance. This may be attributed to the fact that Mo is prone to produce dense passivation films. In addition, the formation of the  $\sigma$  phase increases the corrosion resistance of the coating, but its dispersion distribution reduces the corrosion resistance of the coating. It is generally believed that  $Al_2O_3$  can effectively resist chloride ion corrosion because of its compact structure. However, increasing the Al content further increases the differences in the content of different metal oxides in the passivation film, which will reduce the coating's corrosion resistance. To date, a definitive understanding of the effect of oxide interaction in passive film on the corrosion resistance of HEAs is yet to emerge. However, the data presented in this paper can provide more important information for other researchers in this emerging field.

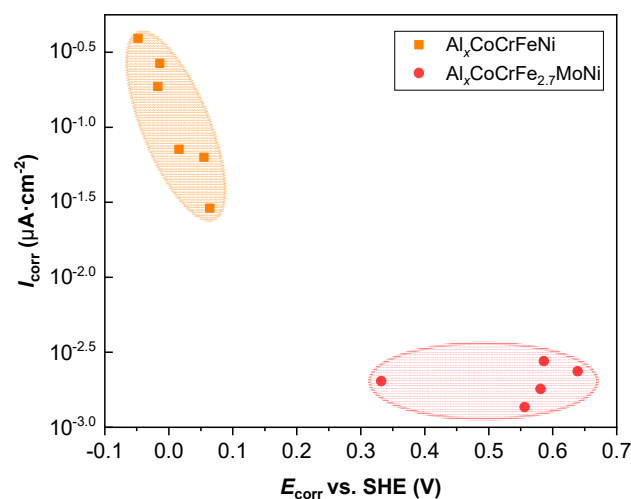


**Figure 10.** Comparison of the corrosion properties of  $Al_xCoCrFe_{2.7}NiMo$  HEAs and  $Al_xCoCrFeNi$  HEAs in a 3.5 wt.% NaCl solution.

## 5. Conclusions

$Al_xCoCrFe_{2.7}MoNi$  coatings were prepared on pure iron via laser cladding, and their microstructure, hardness, wear resistance and corrosion resistance were studied.

The increase of Al content promotes the releasing of Mo from Mo-rich BCC1 phase, and the formation of the (Mo, Cr)-rich  $\sigma$  phase. The increase of Al content causes the increase in volume fraction of BCC2 phase, and correspondingly the increase of hardness and wear resistance. The formation of the strip-shaped  $\sigma$  phase contributes to the improvement of the corrosion resistance of the coating, but the dispersed distribution of the  $\sigma$  phase deteriorates corrosion resistance.

**Author Contributions:** Conceptualization, M.S. (Minghong Sha), C.J. and S.L.; Funding acquisition, M.S. (Minghong Sha) and S.L.; Formal analysis, C.J.; Investigation, C.J.; Resources, W.F., X.A., Y.-A.J. and M.S. (Minggang Shen); Writing - original draft, C.J.; Writing - review & editing, C.J., M.S. (Minghong Sha) and J.Q.

**Funding:** This work was financially supported by the National Key Research and Development Program of China (NO.2017YFB0304201), National Natural Science Foundation of China (NO.51774179), Natural Science Foundation of Liaoning Province (NO.20180550546, NO.20170540460), and the Innovation Team Project of Liaoning Education Department (NO.LT2016003).

**Conflicts of Interest:** The authors declare no conflict of interest.

## References

1. Yeh, J.W.; Chen, S.K.; Lin, S.J.; Gan, J.Y.; Chin, T.S.; Shun, T.T.; Tsau, C.H.; Chang, S.Y. Nanostructured high-entropy alloys with multiple principal elements: Novel alloy design concepts and outcomes. *Adv. Eng. Mater.* **2004**, *6*, 299–303. [[CrossRef](#)]
2. Senkov, O.N.; Wilks, G.B.; Miracle, D.B.; Chuang, C.P.; Liaw, P.K. Refractory high-entropy alloys. *Intermetallics* **2010**, *18*, 1758–1765. [[CrossRef](#)]
3. Miracle, D.B.; Miller, J.D.; Senkov, O.N.; Woodward, C.; Uchic, M.D.; Tiley, J. Exploration and development of high entropy alloys for structural applications. *Entropy* **2014**, *16*, 494–525. [[CrossRef](#)]
4. Yeh, J.W. Alloy design strategies and future trends in high-entropy alloys. *JOM* **2013**, *65*, 1759–1771. [[CrossRef](#)]
5. Zhang, Y.; Zuo, T.T.; Tang, Z.; Gao, M.C.; Dahmen, K.A.; Liaw, P.K.; Lu, Z.P. Microstructures and properties of high-entropy alloys. *Prog. Mater. Sci.* **2014**, *61*, 1–93. [[CrossRef](#)]
6. Gao, M.C.; Liaw, P.K.; Yeh, J.W.; Zhang, Y. *High-Entropy Alloys: Fundamentals and Applications*; Springer: Berlin, Germany, 2016.
7. Lu, Y.; Dong, Y.; Guo, S.; Jiang, L.; Kang, H.; Wang, T.; Wen, B.; Wang, Z.; Jie, J.; Cao, Z. A promising new class of high-temperature alloys: Eutectic high-entropy alloys. *Sci. Rep.* **2014**, *4*, 6200. [[CrossRef](#)]
8. Lei, Z.; Liu, X.; Wu, Y.; Wang, H.; Jiang, S.; Wang, S.; Hui, X.; Wu, Y.; Gault, B.; Kontis, P.; et al. Enhanced strength and ductility in a high-entropy alloy via ordered oxygen complexes. *Nature* **2018**, *563*, 546–550. [[CrossRef](#)]
9. Huang, H.; Wu, Y.; He, J.; Wang, H.; Liu, X.; An, K.; Wu, W.; Lu, Z. Phase-transformation ductilization of brittle high-entropy alloys via metastability engineering. *Adv. Mater.* **2017**, *29*, 1701678. [[CrossRef](#)]
10. He, J.Y.; Wang, H.; Huang, H.L.; Xu, X.D.; Chen, M.W.; Wu, Y.; Liu, X.J.; Nieh, T.G.; An, K.; Lu, Z.P. A precipitation-hardened high-entropy alloy with outstanding tensile properties. *Acta Mater.* **2016**, *102*, 187–196. [[CrossRef](#)]
11. Lu, Y.; Gao, X.; Jiang, L.; Chen, Z.; Wang, T.; Jie, J.; Kang, H.; Zhang, Y.; Guo, S.; Ruan, H.; et al. Directly cast bulk eutectic and near-eutectic high entropy alloys with balanced strength and ductility in a wide temperature range. *Acta Mater.* **2017**, *124*, 143–150. [[CrossRef](#)]
12. Lu, Y.; Jiang, H.; Guo, S.; Wang, T.; Cao, Z.; Li, T. A new strategy to design eutectic high-entropy alloys using mixing enthalpy. *Intermetallics* **2017**, *91*, 124–128. [[CrossRef](#)]
13. Zhang, S.; Wu, C.L.; Zhang, C.H.; Guan, M.; Tan, J.Z. Laser surface alloying of FeCoCrAlNi high-entropy alloy on 304 stainless steel to enhance corrosion and cavitation erosion resistance. *Opt. Laser. Technol.* **2016**, *84*, 23–31. [[CrossRef](#)]
14. Niu, X.; Julius, J.; Dan, Z.; Yang, G.; You, Y. Microstructure and corrosion properties of  $\text{Al}_x\text{FeCoCrNiCu}$  ( $x=0.25, 0.5, 1.0$ ) thin coatings on steel substrates deposited by electron beam evaporation. *Rare Metal Mater. Eng.* **2017**, *46*, 3621–3625. [[CrossRef](#)]
15. Kao, Y.F.; Lee, T.D.; Chen, S.K.; Chang, Y.S. Electrochemical passive properties of  $\text{Al}_x\text{CoCrFeNi}$  ( $x = 0, 0.25, 0.50, 1.00$ ) alloys in sulfuric acids. *Corros. Sci.* **2010**, *52*, 1026–1034. [[CrossRef](#)]

16. Li, Q.H.; Yue, T.M.; Guo, Z.N.; Lin, X. Microstructure and corrosion properties of AlCoCrFeNi high entropy alloy coatings deposited on AISI 1045 steel by the electrospark process. *Metall. Mater. Trans. A* **2013**, *44*, 1767–1778. [[CrossRef](#)]
17. Qiao, J.W.; Ma, S.G.; Huang, E.W.; Chuang, C.P.; Liaw, P.K.; Zhang, Y. Microstructural characteristics and mechanical behaviors of AlCoCrFeNi high-entropy alloys at ambient and cryogenic temperatures. *Mater. Sci. Forum.* **2011**, *688*, 419–425. [[CrossRef](#)]
18. Sun, R.; Zhang, W.; Fu, H. Effect of solid aluminization on microstructure of AlCoCrFeNi high-entropy alloy. *Heat. Treat. Met.* **2015**, *29*, 250–252. [[CrossRef](#)]
19. Manzoni, A.; Daoud, H.; Völkl, R.; Glatzel, U.; Wanderka, N. Phase separation in equiatomic AlCoCrFeNi high-entropy alloy. *Ultramicroscopy* **2013**, *132*, 212–215. [[CrossRef](#)]
20. Ma, S.G.; Zhang, Y. Effect of Nb addition on the microstructure and properties of AlCoCrFeNi high-entropy alloy. *Mat. Sci. Eng. A* **2012**, *532*, 480–486. [[CrossRef](#)]
21. Na, Y.S.; Lim, K.R.; Chang, H.J.; Kim, J. Effect of trace additions of Ti on the microstructure of AlCoCrFeNi-based high entropy alloy. *Sci. Adv. Mater.* **2016**, *8*, 1984–1988. [[CrossRef](#)]
22. Yong, D.; Zhou, K.; Lu, Y.; Gao, X.; Wang, T.; Li, T. Effect of vanadium addition on the microstructure and properties of AlCoCrFeNi high entropy alloy. *Mater. Des.* **2014**, *57*, 67–72. [[CrossRef](#)]
23. Cunat, P. *Alloying Elements in Stainless Steel and Other Chromium-Containing Alloys*; ICDA: Paris, France, 2004.
24. Li, X.C.; Dou, D.; Zheng, Z.Y.; Li, J.C. Microstructure and properties of FeAlCrNiMo<sub>x</sub> high-entropy alloys. *J. Mater. Eng. Perform.* **2016**, *25*, 2164–2169. [[CrossRef](#)]
25. Jiang, L.; Cao, Z.Q.; Jie, J.C.; Zhang, J.J.; Lu, Y.P.; Wang, T.M.; Li, T.J. Effect of Mo and Ni elements on microstructure evolution and mechanical properties of the CoFeNi<sub>x</sub>VMo<sub>y</sub> high entropy alloys. *J. Alloy. Compd.* **2015**, *689*, 585–590. [[CrossRef](#)]
26. Yong, D.; Lu, Y.; Kong, J.; Zhang, J.; Li, T. Microstructure and mechanical properties of multi-component AlCrFeNiMo<sub>x</sub> high-entropy alloys. *J. Alloy. Compd.* **2013**, *573*, 96–101. [[CrossRef](#)]
27. Liu, W.H.; Lu, Z.P.; He, J.Y.; Luan, J.H.; Wang, Z.J.; Liu, B.; Yong, L.; Chen, M.W.; Liu, C.T. Ductile CoCrFeNiMo<sub>x</sub> high entropy alloys strengthened by hard intermetallic phases. *Acta Mater.* **2016**, *116*, 332–342. [[CrossRef](#)]
28. Tsai, M.H.; Yuan, H.; Cheng, G.M.; Xu, W.Z.; Jiang, W.W. Significant hardening due to the formation of a sigma phase matrix in a high entropy alloy. *Intermetallics* **2013**, *33*, 81–86. [[CrossRef](#)]
29. Wei, W.; Li, J.; Hui, J.; Pan, X.; Cao, Z.; Deng, D.; Wang, T.; Li, T. Phase evolution and properties of Al<sub>2</sub>CrFeNiMo<sub>x</sub> high-entropy alloys coatings by laser cladding. *J. Therm. Spray. Technol.* **2015**, *24*, 1333–1340. [[CrossRef](#)]
30. Chou, H.P.; Chang, Y.S.; Chen, S.K.; Yeh, J.W. Microstructure, thermophysical and electrical properties in Al<sub>x</sub>CoCrFeNi (0 ≤ x ≤ 2) high-entropy alloys. *Mat. Sci. Eng. B* **2009**, *163*, 184–189. [[CrossRef](#)]
31. Tong, C.J.; Chen, M.R.; Yeh, J.W.; Lin, S.J.; Chen, S.K.; Shun, T.T.; Chang, S.Y. Mechanical performance of the Al<sub>x</sub>CoCrCuFeNi high-entropy alloy system with multiprincipal elements. *Metall. Mater. Trans. A* **2005**, *36*, 1263–1271. [[CrossRef](#)]
32. Kao, Y.F.; Chen, T.J.; Chen, S.K.; Yeh, J.W. Microstructure and mechanical property of as-cast, -homogenized, and -deformed Al<sub>x</sub>CoCrFeNi (0 ≤ x ≤ 2) high-entropy alloys. *J. Alloy. Compd.* **2009**, *488*, 57–64. [[CrossRef](#)]
33. Takeuchi, A.; Inoue, A. Classification of bulk metallic glasses by atomic size difference, heat of mixing and period of constituent elements and its application to characterization of the main alloying element. *Mater. Trans.* **2005**, *46*, 2817–2829. [[CrossRef](#)]
34. Shi, Y.; Collins, L.; Rui, F.; Zhang, C.; Balke, N.; Liaw, P.K.; Yang, B. Homogenization of Al<sub>x</sub>CoCrFeNi high-entropy alloys with improved corrosion resistance. *Corros. Sci.* **2018**, *133*, 120–131. [[CrossRef](#)]

